Production of molecularly imprinted polymer particles with amide-decorated cavities for CO₂ capture using membrane emulsification/suspension polymerisation

Seyed Ali Nabavi[†], Goran T. Vladisavljević*[‡], Agni Wicaksono[‡], Stella Georgiadou[‡], Vasilije Manović*[†]

[†]Combustion and CCS Centre, Cranfield University, Cranfield, MK43 0AL, United Kingdom.

[‡]Department of Chemical Engineering, Loughborough University, Loughborough LE11 3TU, United Kingdom.

*Corresponding author. Tel: +44 (0)1509 222518; E-mail address:

g.vladisavljevic@lboro.ac.uk (G.T. Vladisavljević).

*Corresponding author: Tel.: +44 (0)1234 754649; E-mail address:

v.manovic@cranfield.ac.uk (V. Manović).

Graphical abstract

Membrane Emulsification → Suspension Polymerisation → Synthesised MIP particles → CO_2 capture breakthrough curves
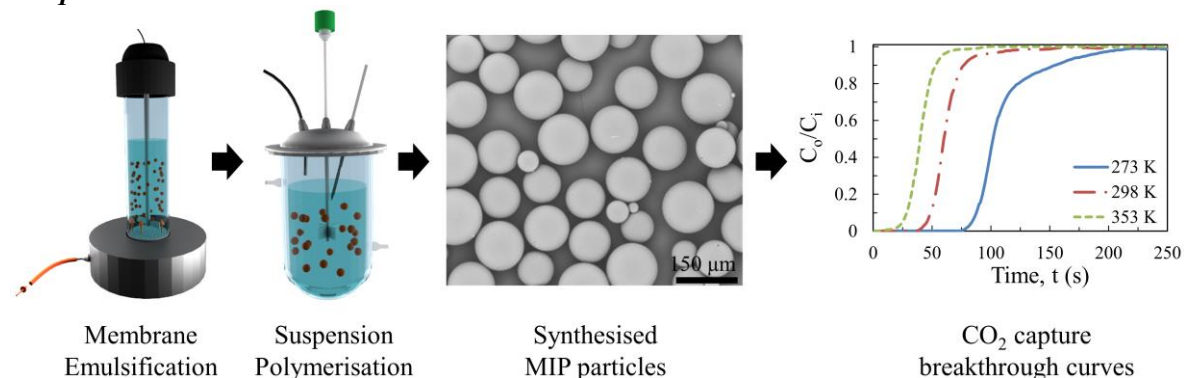
ABSTRACT

Highly uniform amide-based molecularly imprinted polymer (MIP) particles containing CO_2-philic cavities decorated with amide groups were produced using membrane emulsification and subsequent suspension polymerisation. The organic phase containing acrylamide (functional monomer), oxalic acid (dummy template), ethylene glycol dimethacrylate (crosslinker) and azobisisobutyronitrile (initiator) dissolved in a 50/50 mixture (by volume) of acetonitrile and toluene (porogenic solvents) was injected through a microengineered nickel membrane with a pore diameter of 20 μm and a pore spacing of 200 μm into agitated 0.5 wt% aqueous solution of poly(vinyl alcohol) to form droplets that have been polymerised at 60 °C for 3 h. The volume median diameter of the droplets was controlled between 35 and 158 μm by shear stress at the membrane surface. The droplets maintained their physical stability during storage for 4 weeks and their size was independent of the dispersed phase content. The particle size after polymerisation was consistent with the initial droplet size. The

2

particles were stable up to 210 °C and had a specific surface area of 239 m^2/g and a CO_2 capture capacity of 0.59 mmol/g at 273 K and 0.15 bar CO_2 partial pressure.

Keywords: CO_2 capture capacity, molecularly imprinted polymer, amide decorated cavities, membrane emulsification, suspension polymerisation, acrylamide.

1. INTRODUCTION

The increased level of CO_2 in the atmosphere due to excessive combustion of fossil fuels is one of the main causes of global warming and climate change [1,2]. Capture of CO_2 from large point sources and sequestration in geological formations is considered as the most viable short-term solution for reducing the level of CO_2 in the atmosphere [3]. Currently, post-combustion carbon capture by amine scrubbing is the most established technology for the removal of CO_2 from flue gases [4]. However, amine solutions are corrosive and degrade into toxic products after repetitive regeneration cycles at elevated temperatures [5,6]. In addition, amine scrubbing systems exhibit a low specific interfacial area and require high regeneration energy, which can reduce energy output of the plant by 25-40% [7,8].

Solid adsorbents can be attractive alternatives, because they are nontoxic, nonvolatile and noncorrosive, require lower regeneration energy, and display a higher surface area-to-volume ratio [7,9]. Zeolites can have a high CO_2 capture capacity and high CO_2-over-N_2 selectivity under atmospheric conditions [10,11]. However, the presence of moisture in flue gases greatly reduces their capture capacity and requires higher regeneration temperatures, resulting in higher energy penalties [12].

18 Metal organic frameworks (MOFs) show high CO_2 capture capacity at elevated pressures

19 [13], but under typical conditions of post-combustion carbon capture, their capture capacity is

20 reduced, especially in the presence of moisture, NO_x and SO_x [10,14]. Carbonaceous

21 materials are cheap and stable in the presence of moisture and impurities [15]. However, they

22 display a low selectivity for CO_2 over N_2 due to the physisorption mechanism of CO_2 capture

23 [2]. One of the main drawbacks of highly porous materials such as activated carbon and

24 MOFs is their low density, which can limit their application in fluidised bed systems [15,16].

25 Physical impregnation or covalent tethering of amines inside mesopores is an effective way

26 of increasing both CO_2 capture capacity and selectivity of porous CO_2 adsorbents [17,18].

27 CO_2 has a higher affinity towards polar amine or amide groups than other flue gases, due to

28 its larger quadrupole moment and polarisability [19].

29 Polymer-based materials, such as hyper cross-linked polymers (HCPs), porous aromatic

30 frameworks (PAFs), and covalent organic polymers (COPs) are new classes of CO_2

31 adsorbents characterised by a high CO_2 selectivity and capture capacity, high hydrothermal

32 stability and ease of surface modification [20–22]. Acrylamide-based molecularly imprinted

33 polymer (MIP) particles for CO_2 capture with a separation factor of up to 340 at a CO_2 partial

34 pressure of 15 kPa have been fabricated using bulk polymerisation [23]. MIPs contain

35 inherently functionalised nanocavities, which are complementary in shape to the target

36 molecule, and can act as active sites for capturing the target molecules (Fig. 1). Unlike amine

37 impregnation or tethering, which often leads to reduction in the total pore volume and

38 specific surface area of the particles [24], molecular imprinting increases porosity of the

39 particles, leading to a higher rate of diffusion of CO_2 to active sites [23,25].

However, bulk polymerisation is not suitable for large-scale production, because the resulting bulk polymer must be crushed, ground, and sieved to obtain particles of optimum size, which is time-consuming, laborious, and expensive, as only 30-40% of the particles can be recovered. In addition, the produced particles have irregular shape and sharp edges and are prone to attrition [25]. Proper shape, size, and surface morphology of the particles are the key factors for the applicability of adsorbents. Adsorbents with very fine particles cannot be directly used in industrial CO_2 capture systems. In a fixed-bed system, fine particles cause excessive pressure drop through the bed, whereas in fluidised and moving bed systems, they can readily be entrained in fluidising gas and are prone to plugging, channelling, and agglomerating [26,27]. Because of these limitations, fine particles are usually used in palletised form, which can block their active sites and reduce CO_2 capture capacity and capture rate.

In suspension polymerisation, each individual monomer droplet represents a miniature batch reactor leading to higher rates of heat transfer and shorter polymerisation times compared with bulk polymerisation [28]. Since crushing and grinding steps are not involved, higher particle yields can be achieved and synthesised particles are regular spheres due to the spherical shape of the monomer droplets. However, traditional "top-down" emulsification methods, e.g. mixing in a stirred tank, typically lead to highly polydispersed droplets whose size cannot easily be controlled. Membrane emulsification is a "bottom-up" approach based on injection of one liquid through a microporous membrane into another immiscible liquid phase, leading to generation of uniform droplets [29]. Continuous membrane emulsification systems enable large-scale production and can involve oscillatory (pulsed) flow of the continuous phase [29,30] or nonstationary membrane, such as rotating [31] or vibrating

[32,33] membrane. Membrane emulsification followed by suspension polymerisation has already been used for preparation of porous and nonporous, coherent and structured, and homogeneous and heterogeneous polymeric particles from various monomers such as styrene, methacrylic acid, dimethylaminoethyl methacrylate, 2-hydroxyethyl methacrylate, methyl methacrylate, and methyl acrylate [34,35].

In this study, membrane emulsification/suspension polymerisation method will be explored for fabrication of spherical molecularly imprinted poly[acrylamide-co-(ethyleneglycol dimethacrylate)] particles with amide-decorated cavities for CO_2 capture. The particles will be characterised by their thermal stability, surface morphology, porosity, and CO_2 capture capacity. The material is highly selective to CO_2 due to shape specificity of the cavities and the presence of amide groups covalently incorporated within the 3D network of the polymer.
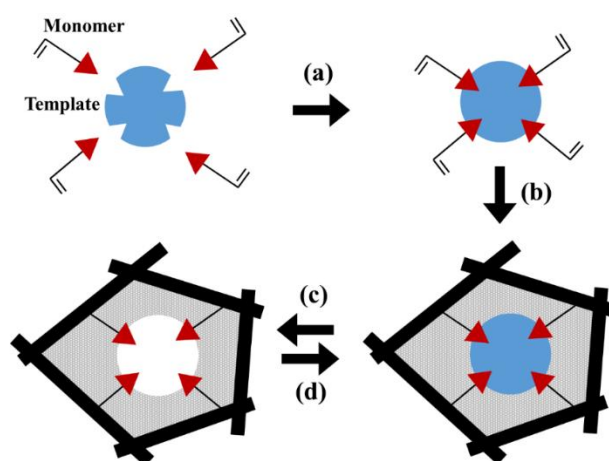

Fig. 1. Formation of molecularly imprinted polymer matrix in this study: (a) Self-assembly of oxalic acid (dummy template) and AAM (monomer); (b) Cross-linking of monomer-template complex using EGDMA; (c) Template removal by methanolic HCl and formation of cavities decorated with amide groups; (d) Capture of CO_2 molecules within the cavity. Template and CO_2 molecules are shown as blue spheres, while amide ($CONH_2$) groups are shown as red triangles.

2. EXPERIMENTAL SECTION

2.1. Materials

Oxalic acid (OA), acrylamide (AAM), acetonitrile (AN), toluene (TL), methanol, and 0.1 M hydrochloric acid were purchased from Fisher Scientific (UK). Ethylene glycol dimethacrylate (EGDMA), azobisisobutyronitrile (AIBN), and polyvinyl alcohol (PVA, M_w = 13,000–23,000, 87–89% hydrolysed) were purchased from Sigma Aldrich (UK). All reagents were of analytical reagent grade. Reverse osmosis (DI) water was supplied using Millipore 185 Milli-Q Plus apparatus. All gases were supplied by BOC (UK) with purity higher than 99.999%.

2.2. Particle Synthesis

The MIP particles were synthesised through the following five steps:

Step 1. Monomer-template self-assembly. A crucial first step in the molecular imprinting process is the self-assembly of functional monomer and template in a pre-polymerised organic phase (Fig. 1a), which enables creation of template-shaped cavities within the polymer matrix. Since CO_2 has a very low solubility in organic solvents under ambient conditions, oxalic acid, a structural analogue of two CO_2 molecules, was used as a dummy template. AAM was selected as a functional monomer, due to high affinity of amide groups towards CO_2. Monomer-template self-assembly occurred in a 50/50 mixture (by volume) of TL and AN using a mass ratio of AAM to OA of 2.27/1. The mass-to-volume ratio of AAM to porogenic solvents (AN and TL) was 1/11.76. The mixture was stirred for 2 h before EGDMA and AIBN were added as a crosslinker and initiator, respectively. The mass ratio of AAM to EGDMA and AAM to AIBN in the organic phase was 1/4.66 and 17/1, respectively. The composition of the organic phase was optimised in our preliminary investigation.

Step 2. Membrane emulsification. The oil-in-water (O/W) emulsion was produced using a commercial Micropore Dispersion Cell (MDC) equipped with a flat disc membrane and a paddle-blade stirrer driven by a 24 V DC motor (Fig. 2a). The organic phase was injected at a constant flow rate through the membrane into 50 mL of a 0.5 wt% aqueous solution of PVA using a syringe pump (World Precision Instruments, Sarasota, US). The paddle stirrer fitted above the membrane provided an adjustable shear on the membrane surface to control the droplet size. A nickel membrane containing hexagonal arrays of cylindrical pores with a diameter of 20 µm and a pore spacing of 200 µm was fabricated by the LIGA (LIthographie, Galvanik und Abformung) process, which is based on lithography, nickel electroplating and moulding. The membrane and MDC were supplied by Micropore Technologies Ltd (Redcar, UK).

Once the desired amount of oil phase passed through the membrane, the emulsion droplets were transferred to the reactor and polymerised. The membrane was cleaned by immersing in a 15 vol% NaOH for 10 min, followed by 10 min soaking in 7 vol% citric acid and 20 min treatment with DI water in an ultrasonic bath at 30°C.

Step 3. Suspension polymerization. The O/W emulsion produced in Step 2 was poured into a preheated 500-mL jacketed reactor equipped with a four-neck lid and a four-blade impeller with a diameter of 50 mm (Fig. 2b). The polymerisation took 3 h at an agitation rate of 75 rpm and 60°C. The temperature was controlled using a water recirculating heater/chiller system. The emulsion was purged with N_2 for 10 min prior to the reaction, after which nitrogen blanketing was used to prevent the presence of oxygen within the reaction mixture.

Step 4. Surfactant removal. After polymerisation, the suspension was filtered using a Buchner funnel apparatus with a filter paper (Gard 3, Whatman 6 µm), and the particles were

122   washed with DI water at 85-90°C for 5 min in a water bath while stirring. The washing was

123   repeated 8-10 times until PVA was completely removed from the particles. If the surfactant

124   was not completely removed, the particles were highly agglomerated. The particle

125   agglomeration was investigated by taking SEM images of the washed particles. After

126   complete removal of the surfactant, the particle agglomeration was negligible. Once the

127   washing procedure was optimised, SEM imaging was not necessary.

128   ***Step 5. Template removal.*** OA was extracted from the particles by washing the sample with a

129   10/90 mixture (by volume) of hydrochloric acid and methanol, until no OA was detected in

130   the rinses by a Lambda 35 UV/VIS spectrometer (PerkinElmer, US). Finally, the particles

131   were washed with DI water and dried overnight in a vacuum oven at 80°C. The removal of

132   OA from the polymer matrix created cavities decorated with $CONH_2$ groups capable of

133   binding CO_2 via Lewis acid-base type interactions (Fig. 1d). It should be noted that the

134   cavities created by molecular imprinting differ from the pores formed by phase separation

135   between polymer and solvent during polymerisation. The size of the cavities is similar to that

136   of the template molecules (< 1 nm), while the pores are larger and lie in a mesoscale range

137   (2-50 nm).
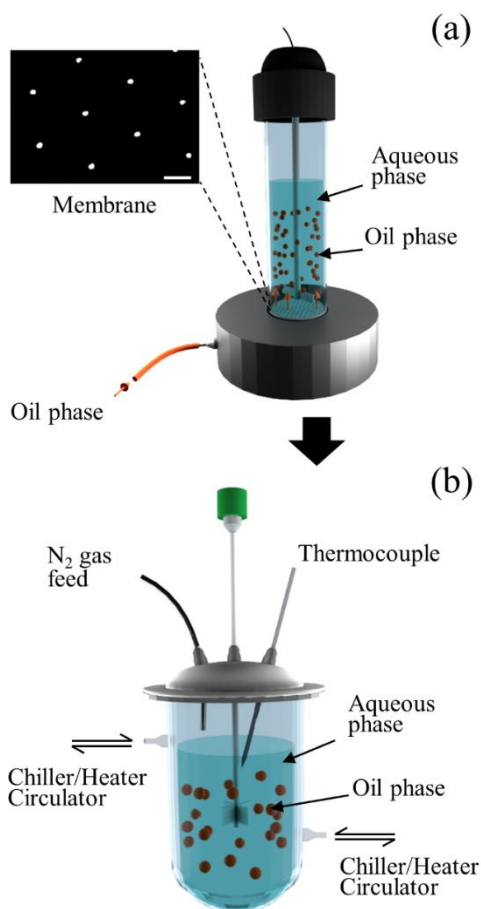
138

Fig. 2. A schematic of the experimental set-up for the production of MIP particles: (a) Micropore Dispersion Cell for membrane emulsification of the organic phase (AAM, OA, EGDMA, and AIBN dissolved in a mixture of AN and TL) into a 0.5 wt% PVA solution. The inset image is a micrograph of the membrane surface, and the scale bar is 100 µm; (b) Jacketed batch reactor for suspension polymerisation at controlled temperature.

139

140 ## 2.3. Material Characterization

141

142 ***Scanning Electron Microscopy (SEM).*** The particle morphology was evaluated using a

143 TM3030 bench-top Scanning Electron Microscope (Hitachi, Tabletop Microscope Europe)

144 operating at an accelerating voltage of 15 keV. The accumulation of electrostatic charges on

145 the particles was prevented by coating the samples with gold/palladium (80/20) prior to SEM

146 measurements. The sputter coating speed was 0.85 nm per second at an applied voltage of 2

147 kV and a plasma current of 25 mA.

148 ***Pore size analysis.*** The pore size analysis of the samples was performed using an ASAP 2020

149 Micromeritics Accelerated Surface Area and Porosimetry system at 77 K within a liquid

150 nitrogen bath. Prior to each measurement, the samples were degassed at 80°C overnight. The

151 Brunauer–Emmett–Teller (BET) model was used to estimate the specific surface area over a

152 range of relative pressures, P/P_0, of 0.06-0.3. The Barrett-Joyner-Halenda (BJH) model was

153 used to determine the pore size distribution, and the total pore volume was obtained from the

154 amount of N_2 adsorbed at P/P_0 of 0.99.

155 ***Thermal analysis.*** The thermal stability of the samples was investigated using a

156 thermogravimetric analyser (TGA) (Q5000 IR, TA Instruments, US). In each test, 10-20 mg

157 of the sample was heated from 50 to 600°C at a ramp rate of 10°C/min under a nitrogen flow

158 rate of 20 mL/min.

159 ***Density measurement.*** The particle density was measured using a helium pycnometer

160 (Micromeritics, US), over five runs and the average value was reported. The samples were

161 dried overnight in a vacuum oven at 80°C prior to the test.

162 ***Particle size analysis.*** The droplet and particle size distribution were measured using a laser

163 diffraction particle size analyser (Malvern Mastersizer S, Malvern Instruments, UK). The

164 average size was expressed as the volume median diameter, $D_{v,0.5}$, corresponding to 50 vol%

165 on the cumulative particle size distribution curve. The particle (droplet) size uniformity was

166 estimated using a relative span factor given by

$$\text{span} = \frac{D_{v,0.9} - D_{v,0.1}}{D_{v,0.5}} \tag{1}$$

167 where $D_{v,0.9}$ and $D_{v,0.1}$ are the diameters corresponding to 90 and 10 vol% of the particles,

168 respectively.

169 ***CO2 capture.*** The CO_2 capture capacity of the particles was measured using a fixed-bed

170 adsorption column (15.8 mm O.D. and 9.25 mm I.D., stainless steel). A schematic of the rig

171 is shown in Fig. 3. In each test the column was packed with 3 g of the particles. A stainless

172 steel mesh with an average pore size of 0.075 mm and quartz wool plugs were placed at both

173 sides of the column to prevent particles from escaping from the bed and contaminating the

174 system. A uniform temperature distribution over the bed was achieved using an in-house

175 temperature controller system. The gas flow rate was controlled by a mass flow controller

176 (Alicat Scientific Inc, UK). Prior to each test, the column was purged with 130 mL/min of N_2

177 for 2 h at 120°C and then allowed to cool down to the test temperature. The CO_2 capture was

178 done by blowing through the bed a simulated gas mixture of CO_2 and N_2 containing 15 %

179 (v/v) N_2 at 130 mL/min. The CO_2 concentration in the effluent stream was continuously

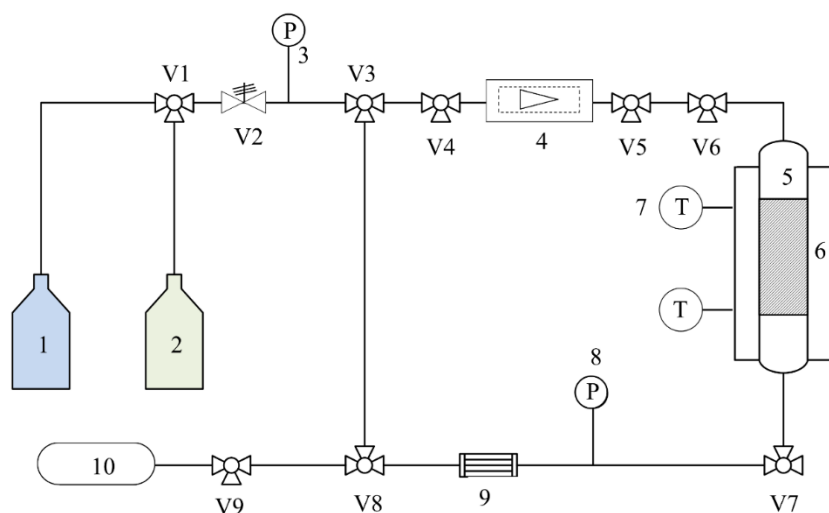180 monitored using a CO_2 infrared analyser (Quantek Instruments, USA).

Fig. 3. A schematic of the rig used to test CO_2 capture capacity of the synthetised MIP particles: (1) CO_2 cylinder; (2) N_2 cylinder; (3 & 8) pressure gauge; (4) mass flow controller; (5) fixed bed column; (6) heating system; (7) thermocouples; (9) Peltier cooling module; (10) CO_2 gas analyser; (V1 & V3-V9) 3-way valves; (V2) relief valve.
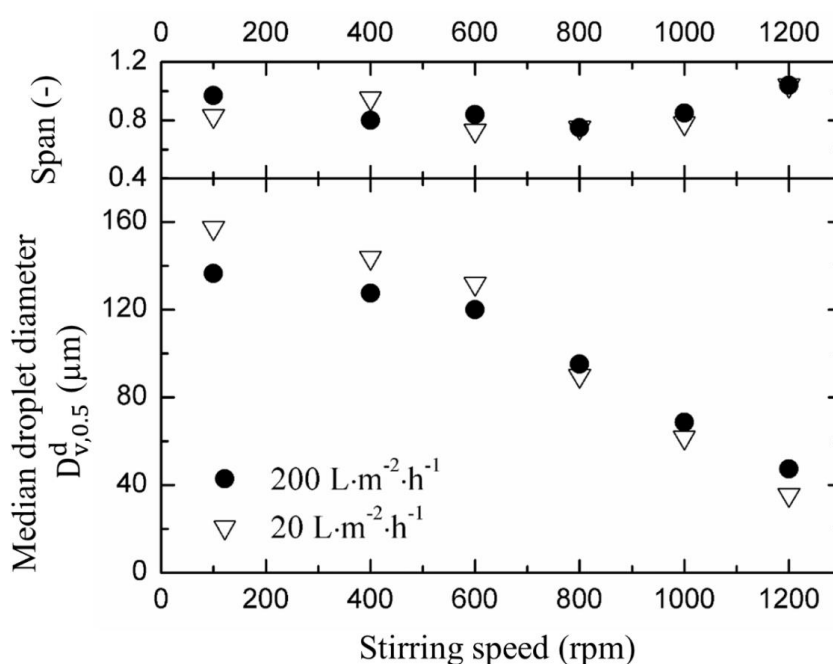
181 # 3. RESULTS AND DISCUSSION

182

183 ## 3.1. Membrane emulsification

184

Fig. 4. The effect of stirring rate during membrane emulsification on the volume median diameter, $D_{v,0.5}^d$, and the span at $J_d = 20$ and 200 $Lm^{-2}h^{-1}$. The dispersed (oil) phase content ϕ_o at the end of the emulsification process was 9 vol%.

185

186

187 Fig. 4 shows the effect of stirring rate in the MDC on the volume median droplet diameter,

188 $D_{v,0.5}^d$, and span at the transmembrane flux of 20 and 200 $Lm^{-2}h^{-1}$. The dispersed phase

189 content at the end of the process was 9 vol%. An increase in stirring speed from 100 to 1200

190 rpm caused a reduction in $D_{v,0.5}^d$ from 157 to 34 µm at 20 $Lm^{-2}h^{-1}$, and from 137 to 47 µm at

191 200 $Lm^{-2}h^{-1}$. For membrane with a hexagonal pore array, $D_{v,0.5}^d$ can be correlated with the

192 droplet formation time, t_d and the transmembrane flux, J_d, using the following equation [36]:

$$D_{v,0.5}^d = (\frac{3\sqrt{3}}{\pi k}J_d L^2 t_d)^{1/3} \qquad (2)$$

193 where L is the membrane pore spacing and k is the fraction of active pores. At constant J_d

194 and k values, an increase in stirring rate leads to an increase in the drag force acting on the

195 droplets during formation on the membrane surface and the droplet formation time is shorter,

196 causing a reduction in $D_{v,0.5}^d$ based on Eq. (2). The effect of flux on $D_{v,0.5}^d$ differs depending

197 on the rotational speed of the stirrer. At higher stirring rates (800-1200 rpm), the droplets are

198 smaller and do not touch each other while they are growing on the membrane surface. In this

199 case, at higher dispersed phase flux, a higher amount of the dispersed phase will flow into the

200 growing droplet during pinch off and larger droplets will be formed (Fig. 4). At lower stirring

201 rates (100-600 rpm), the size of adjacent growing droplets may become comparable with the

202 membrane pore spacing ($D_{v,0.5}^d \approx L$), causing the forming drops to teach each other on the

203 membrane surface and exert an additional force, the push-off force [37]. The push-off force

204 arises from droplet deformation and acts normal to and away from the membrane surface, i.e.,

205 in the opposite direction to the interfacial tension force, leading to shorter droplet formation

206 time and lower $D_{v,0.5}^d$ values at higher fluxes. As shown in Fig. 4, the most uniform droplets

207 with a span below 0.8 were obtained at the intermediate rotation speeds (600 and 800 rpm).
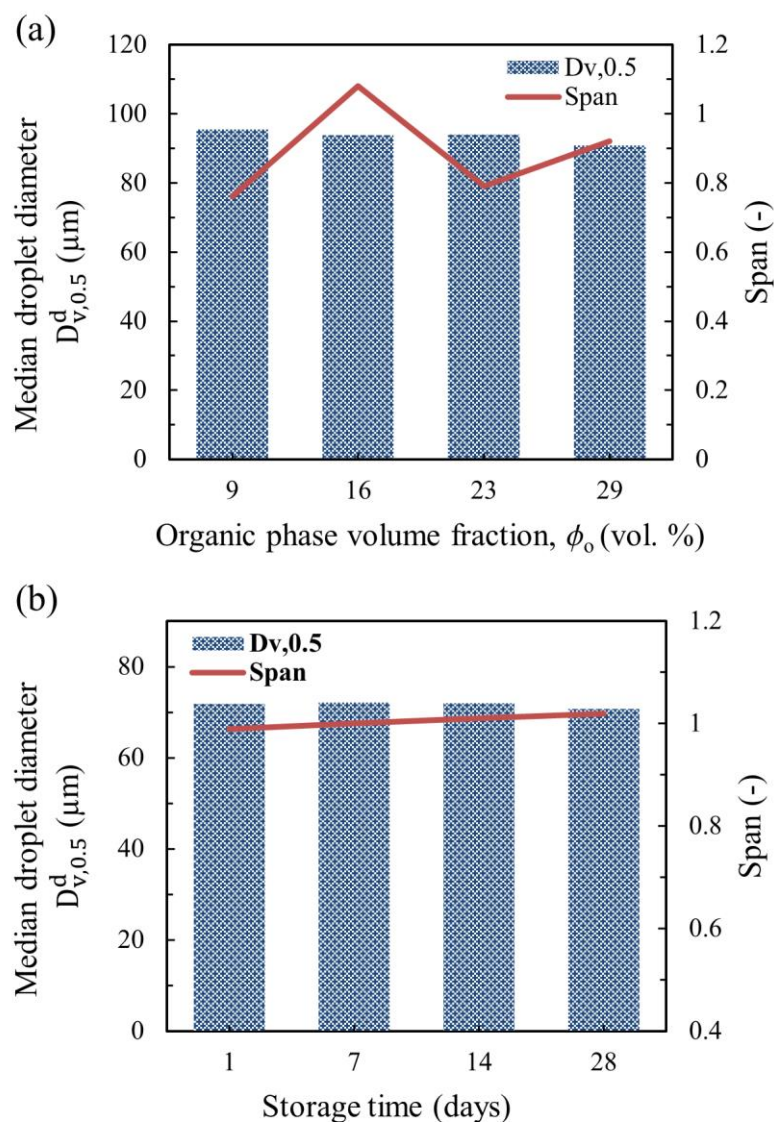
Fig. 5. (a) The effect of dispersed phase content on the volume median diameter, $D^d_{v,0.5}$, and the span at a stirring rate of 800 rpm and $J_d = 200$ Lm^{-2}h^{-1}. (b) Long-term emulsion stability prior to suspension polymerisation.

208

The effect of dispersed phase content ϕ_o in the prepared emulsion on $D^d_{v,0.5}$ and span at a

stirring rate of 800 rpm and flux of 200 Lm^{-2}h^{-1} is shown in Fig. 5a. No significant variations

in $D^d_{v,0.5}$ were observed when ϕ_o increased from 9% to 29%. The same trend was observed in

preparation of sunflower oil-in-water emulsions stabilised by 2 wt% Tween 20 in the MDC

over a ϕ_o range from 5 to 60% [36]. This behaviour can be attributed to the short injection

15

214   time that ranged from less than 2 min at $\phi_o = 9$ vol% to 7 min at $\phi_o = 29$ vol% during which

215   no significant changes in membrane fouling occurred. The most uniform emulsion droplets

216   with a span of 0.76 were obtained at ϕ_o of 9%. The stability of emulsion droplets against

217   coalescence over 4 weeks of storage at ambient temperature is shown in Fig. 5b. Since AIBN

218   slowly decomposes at room temperature, in this stability study no AIBN was added in the

219   organic phase to prevent polymerisation during storage. No noticeable change in $D_{v,0.5}^d$ was

220   observed over the entire 4-week period implying stable emulsion formulation, although the

221   droplet size uniformity deteriorated slightly over time.
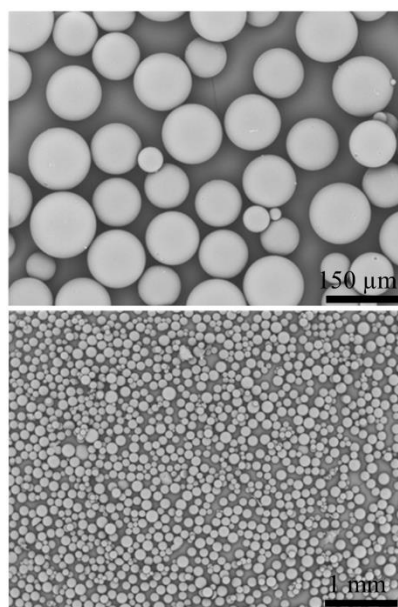
222

223   Fig. 6. SEM images of the MIP particles ($D_{v,0.5}^p = 141$ µm, span = 0.96) taken at different
224   magnifications. The emulsion was prepared at 400 rpm, $J_d = 200$ Lm^{-2}h^{-1}, and $\phi_o = 23$ vol%.
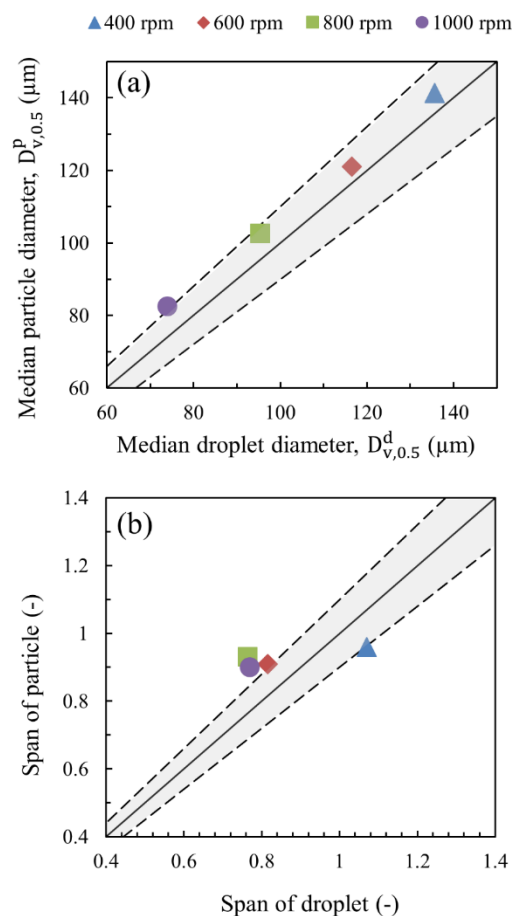225

Fig. 7. A comparison of the median particle diameter (a) and the relative span factor (b)
before polymerisation and after polymerisation and downstream processing. The solid lines
follow the equations (a): $D_{v,0.5}^{p} = D_{v,0.5}^{d}$ and (b): particle span = droplet span. The dashed
lines represent ±10% deviation from the diagonal lines. The emulsions were prepared at J_d
= 200 Lm^{-2}h^{-1} and ϕ_o = 23 vol%.

3.2. Characterisation of synthesised MIP particles

Fig. 6 shows SEM images of produced particles after downstream processing, i.e. surfactant

removal and template extraction. All the particles are non-agglomerated, spherical and have a

smooth surface without cracks. Fig. 7a gives a comparison between the size of the droplets

before polymerisation and the corresponding size of the particles after polymerisation and

washing. All emulsions were prepared with a dispersed phase content of 23 vol% at J_d of 200

Lm^{-2}h^{-1} and 400-1000 rpm. The solid diagonal line indicates the data points for which $D_{v,0.5}^{d}$

is equal to $D_{v,0.5}^{p}$, and the two dashed lines represent ±10% deviation of $D_{v,0.5}^{p}$ from $D_{v,0.5}^{d}$. It

236   can be seen that $D_{v,0.5}^{p}$ deviates from $D_{v,0.5}^{d}$ only by 4% for the largest droplets produced at

237   400 rpm. The deviation of $D_{v,0.5}^{p}$ from $D_{v,0.5}^{d}$ increases with decreasing droplet size and

238   reaches 10% for the smallest droplets produced at 1000 rpm. This observation was not

239   surprising, since very fine particles can be removed during washing, shifting the particle size

240   distribution curve towards the larger particle sizes. The $D_{v,0.1}^{d}$ value for the droplets produced

241   at 1000 and 400 rpm was 49.9 and 71.6 µm, respectively. After polymerisation and washing,

242   the corresponding $D_{v,0.1}^{p}$ values were 66.5 and 83.1 µm (33% and 16% higher than the $D_{v,0.1}^{d}$

243   values), meaning that in the former case the fines were more substantially washed away. Fig.

244   7b shows that the size distribution for the particles is similar to that for the droplets and span

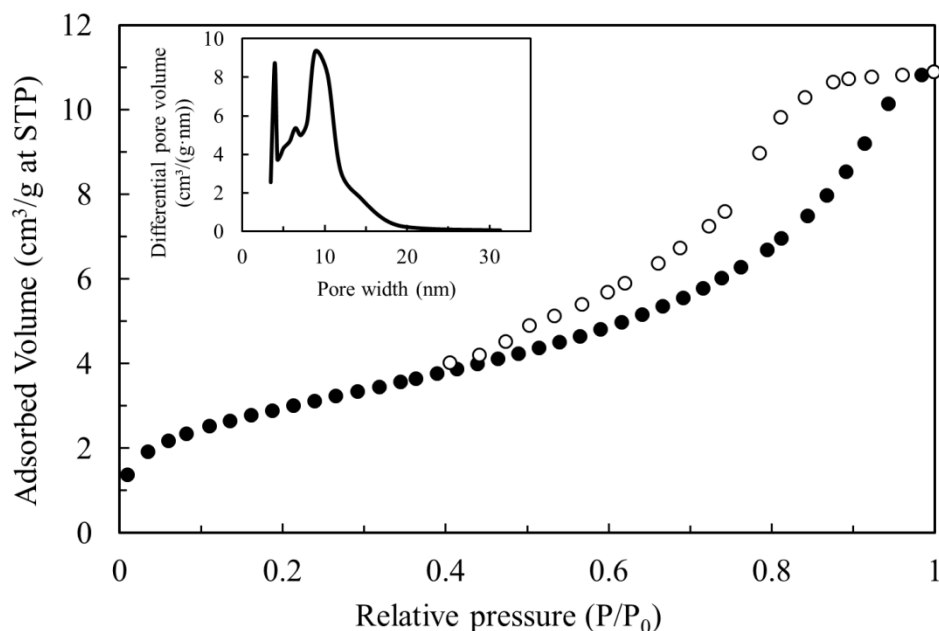245   values for the particles are around 0.9 in all cases.

Fig. 8. Nitrogen adsorption-desorption isotherm of the particles produced from droplets at 800 rpm, 200 Lm^{-2}h^{-1}, and $\phi_o = 23$ vol%. The solid and open symbols denote the adsorption and desorption curve, respectively. The inset graph shows the pore size distribution curve.

Fig. 8 shows a nitrogen adsorption-desorption isotherm and pore size distribution of the particles. The isotherm is characterised by a hysteresis loop between relative pressure, P/P_0, of 0.4 and 0.95 associated with capillary condensation occurring in mesopores, implying a type IV isotherm, according to IUPAC classification [50]. The adsorption volume rapidly increases at low P/P_0 values of less than 0.05 due to strong interaction of the N_2 molecules with a bare surface. When the monolayer formation is completed, multilayer formation starts to take place corresponding to the sharp knee of the isotherm. The specific surface area, S_{BET}, of the sample was 239 m²/g and the pore size distribution was bimodal, with two maxima at diameters of 4 and 9 nm. Compared to MIP particles synthesised by bulk polymerisation that follow a type II adsorption isotherm with an average pore size of 10-24 nm [32], the pore size distribution of the sample in Fig. 8 is considerably narrower with a smaller average pore size.
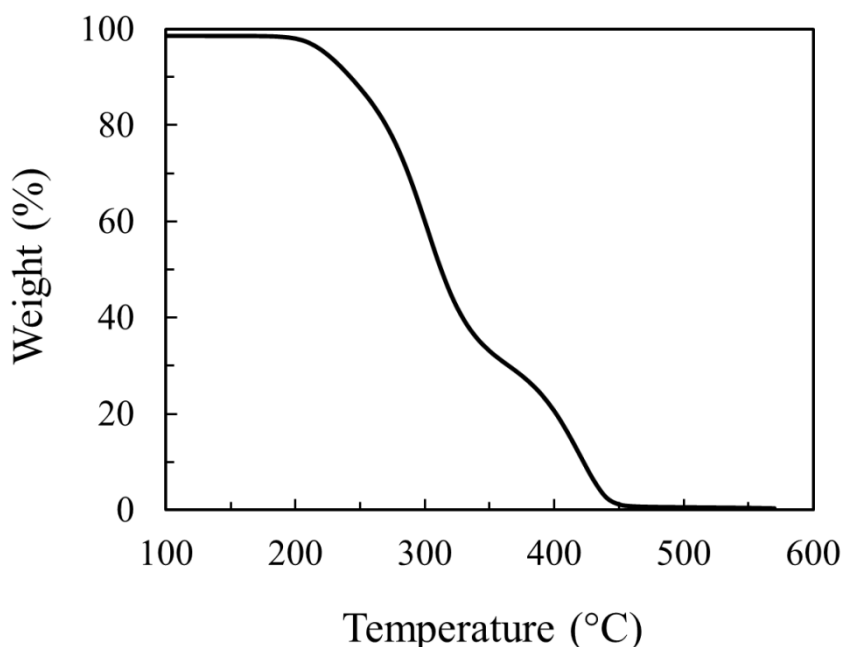

Fig. 9. Thermal degradation of the particles over the temperature range of 100- 600°C at a ramp rate of 10 °C/min and under the nitrogen flow. The monomer droplets were produced at 800 rpm, $J_d = 200$ Lm^{-2}h^{-1}, and $\phi_o = 23$ vol%.

Fig. 9 shows the TGA curve of the sample heated from 100 to 600°C at a ramp rate of 10 °C/min in an inert atmosphere of N_2. There was no obvious weight loss up to 210°C and 5% mass loss occurred at 245°C, which is well above anticipated desorption temperature. The average density of the particles measured with a helium pycnometer was 1.3 g/cm^3. Based on their size and density, the particles belong to group A of the Geldart classification [51], referred to as aeratable particles. These particles can easily be fluidised, with homogeneous fluidisation at low superficial gas velocities and relatively small bubbles at higher velocities [52].
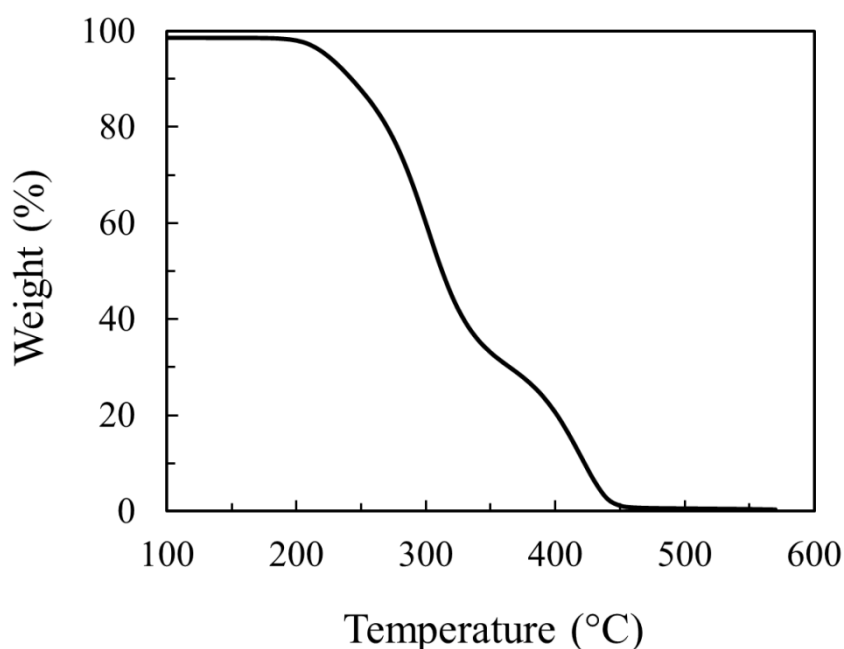

Fig. 9. Thermal degradation of the particles over the temperature range of 100- 600°C at a ramp rate of 10 °C/min and under the nitrogen flow. The monomer droplets were produced at 800 rpm, $J_d = 200$ $Lm^{-2}h^{-1}$, and $\phi_o = 23$ vol%.

246

20

247 Fig. 9 shows the TGA curve of the sample heated from 100 to 600°C at a ramp rate of 10

248 °C/min in an inert atmosphere of N_2. There was no obvious weight loss up to 210°C and 5%

249 mass loss occurred at 245°C, which is well above anticipated desorption temperature. The

250 average density of the particles measured with a helium pycnometer was 1.3 g/cm^3. Based on

251 their size and density, the particles belong to Geldart Group A [39], referred to as aeratable

252 particles. These particles can easily be fluidised, with homogeneous fluidisation at low

253 superficial gas velocities and relatively small bubbles at higher velocities [40].

3.3. CO₂ capture capacity of MIP particles

256 The CO_2 capture capacity of the MIP particles was determined in a fixed-bed reactor at

257 constant adsorption temperatures of 273, 298, and 353 K. The equilibrium CO_2 capture

258 capacity, q_{eq} (mmol/g) was calculated using Eq. (3):

$$q_{eq} = \frac{QC_i t_{ad}}{m_s} \tag{3}$$

259 where Q (mL/min) is the feed gas flow rate, m_s (g) is the mass of the particles in the column,

260 and C_i (mmol/mL) is the molar concentration of CO_2 in the feed stream:

$$C_i = \frac{y_i P}{RT} \tag{4}$$

261 where y_i is the CO_2 molar fraction in the feed stream which was 0.15 in this work, P (kPa) is

262 the total gas pressure in the reactor (~102 kPa), T (K) is the operating temperature, R is the

263 universal gas constant, 8.314 J/(K·mol), and t_{ad} is the stoichiometric time, which is the

264 breakthrough time in an ideal adsorption column with a vertical breakthrough curve. The

265 ideal adsorption column operates at 100% CO_2 removal efficiency until the adsorbent

266 becomes fully saturated with CO_2, after which the removal efficiency instantaneously drops

267 to zero. The breakthrough time is equivalent to the area between the breakthrough curve and

268 the C_o/C_i axis, as shown by the hatched area in Fig. 10, and can be calculated from [41]

$$t_{ad} = \int_0^\infty \left(1 - \frac{C_o}{C_i}\right) dt \qquad (5)$$

269 where C_o (mmol/mL) is the molar concentration of CO_2 in the effluent stream.

T (K)	q_{eq} (mmol/g)
273	0.59
298	0.30
353	0.16
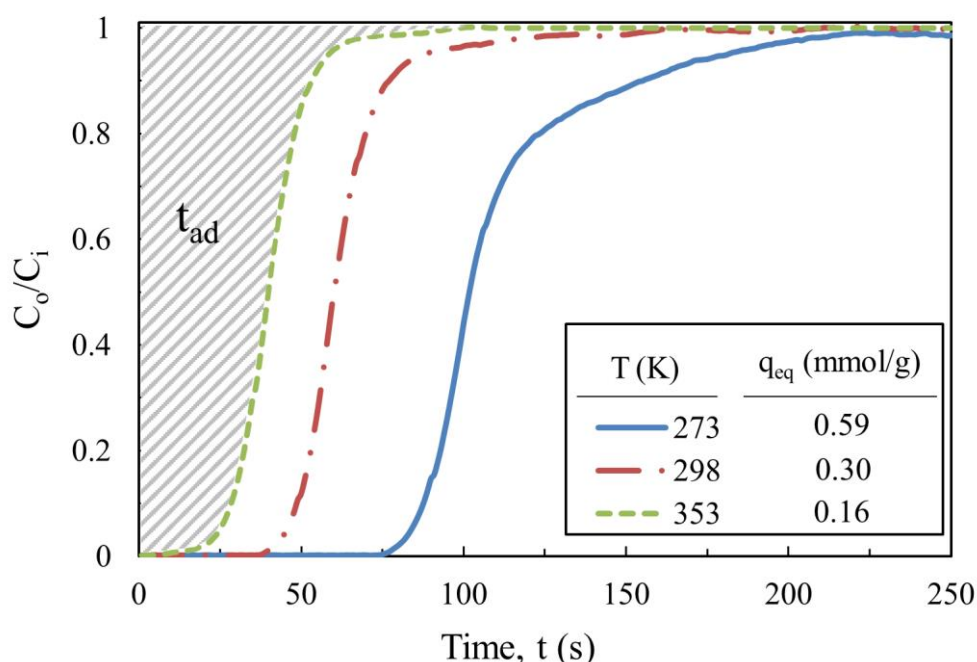
270
271 Fig. 10. The breakthrough curves of the MIP particles at different temperatures. The CO_2
272 partial pressure in the reactor was 0.15 bar. The inset table shows the equilibrium CO_2
273 capture capacity of the particles at different temperatures calculated using Eq. (3). The
274 hatched area corresponds to the stoichiometric time at 253 K. The emulsion was produced at
275 800 rpm, $J_d = 200$ Lm^{-2}h^{-1}, and $\phi_o = 23$ vol%.
276

277 The q_{eq} values determined from the breakthrough curves in Fig. 10 were 0.59, 0.30, and 0.16

278 mmol/g at 273, 298, and 353 K, respectively. These CO_2 capture capacities are comparable to

279 those of N_2-phobic nanoporous azo-covalent organic polymers synthesised by Patel et al.

280 [42]. The lower capture capacities at higher temperatures can be attributed to the exothermic

281 nature of the adsorption process and weaker hydrogen bonding interactions between CO_2

molecules and amide groups within the cavities. The mass transfer resistance in the column can be estimated from the slope of the breakthrough curves in the mass transfer zone [43]. In Fig. 10, the steeper slope of the breakthrough curve at higher temperatures can be attributed to the lower mass transfer resistance, due to faster diffusion of CO_2.

4. CONCLUSIONS

Spherical molecularly imprinted polymeric particles containing $CONH_2$ decorated cavities with CO_2 recognition properties were fabricated using membrane emulsification and subsequent suspension polymerisation. The amide groups of the functional monomer (AAM) stayed intact during polymerisation, meaning that the particles were inherently functionalised with polar amide groups and an additional surface functionalisation step was not necessary. The droplet size was controlled by shear stress at the membrane surface during the membrane emulsification process, associated with varying stirring rate. The size of the particles after polymerisation was consistent with the initial droplet size, but the median particle size increased by 4-10% after washing due to removal of fine particles. The droplets maintained their physical stability during storage for 4 weeks and their size was independent of the dispersed phase content reached at the end of the emulsification process. The nitrogen adsorption-desorption isotherm of the material was of type IV, with pore diameters smaller than 20 nm and a specific surface area of 239 m²/g. Based on their density of 1.3 g/cm^3 and mean diameters of 80-140 µm, the particles were classified into Geldart group A ('aeratable' and easily fluidisable). The particles were thermally stable up to 210°C and exhibited a CO_2 capture capacity of 0.59 mmol/g at 273 K and 0.15 bar CO_2 partial pressure. Future work will be focused on scale-up of the production process using continuous membrane emulsification systems.

ACKNOWLEDGEMENT

REFERENCES

[1]   N. MacDowell, N. Florin, A. Buchard, J. Hallett, A. Galindo, G. Jackson, et al., An overview of CO_2 capture technologies, Energy Environ. Sci. 3 (2010) 1645–1669.

[2]   J. Wang, L. Huang, R. Yang, Z. Zhang, J. Wu, Y. Gao, et al., Recent advances in solid sorbents for CO_2 capture and new development trends, Energy Environ. Sci. 7 (2014) 3478–3518.

[3]   IEA, Technology Roadmap: Carbon capture and storage, Paris, 2013.

[4]   G.T. Rochelle, Amine scrubbing for CO_2 capture, Science 325 (2009) 1652–1654.

[5]   E.F. da Silva, A.M. Booth, Emissions from postcombustion CO_2 capture plants, Environ. Sci. Technol. 47 (2013) 659–660.

[6]   S.K. Akagi, R.J. Yokelson, C. Wiedinmyer, M.J. Alvarado, J.S. Reid, T. Karl, et al., Emission factors for open and domestic biomass burning for use in atmospheric models, Atmos. Chem. Phys. 11 (2011) 4039–4072.

[7]   D.M. D'Alessandro, B. Smit, J.R. Long, Carbon dioxide capture: prospects for new materials, Angew. Chem. Int. Ed. 49 (2010) 6058–6082.

[8]   Y.J. Lin, G.T. Rochelle, Approaching a reversible stripping process for CO_2 capture, Chem. Eng. J. 283 (2016) 1033–1043.

[9]   T.M. McDonald, W.R. Lee, J.A. Mason, B.M. Wiers, C.S. Hong, J.R. Long, Capture of carbon dioxide from air and flue gas in the alkylamine-appended metal-organic framework mmen-Mg_2(dobpdc), J. Am. Chem. Soc. 134 (2012) 7056–7065.

[10]   M.E. Boot-Handford, J.C. Abanades, E.J. Anthony, M.J. Blunt, S. Brandani, N. Mac Dowell, et al., Carbon capture and storage update, Energy Environ. Sci. 7 (2014) 130–189.

[11]   J. Yoo, S.H. Cho, T. Yang, Comparison of activated carbon and zeolite 13X for CO_2 recovery from flue gas by pressure swing adsorption, Ind. Eng. Chem. Res. 34 (1995) 591–598.

[12]   G. Li, P. Xiao, P. Webley, J. Zhang, R. Singh, M. Marshall, Capture of CO_2 from high humidity flue gas by vacuum swing adsorption with zeolite 13X, Adsorption 14 (2008) 415–422.

[13]   M. Eddaoudi, J. Kim, N. Rosi, D. Vodak, J. Wachter, M. O'Keeffe, et al., Systematic design of pore size and functionality in isoreticular MOFs and their application in methane storage, Science 295 (2002) 469–472.

[14]   K. Sumida, D.L. Rogow, J.A. Mason, T.M. McDonald, E.D. Bloch, Z.R. Herm, et al., Carbon dioxide capture in metal-organic frameworks, Chem. Rev. 112 (2012) 724–781.

[15]   S.D. Kenarsari, D. Yang, G. Jiang, S. Zhang, J. Wang, A.G. Russell, et al., Review of recent advances in carbon dioxide separation and capture, RSC Adv. 3 (2013) 22739–22773.

[16]   J. Liu, N. Sun, C. Sun, H. Liu, C. Snape, K. Li, et al., Spherical potassium intercalated activated carbon beads for pulverised fuel CO_2 post-combustion capture, Carbon 94 (2015) 243–255.

[17]   S. Choi, J.H. Drese, P.M. Eisenberger, C.W. Jones, Application of amine-tethered solid sorbents for direct CO_2 capture from the ambient air, Environ. Sci. Technol. 45 (2011) 2420–2427.

[18]   N. Hiyoshi, K. Yogo, T. Yashima, Adsorption of carbon dioxide on amine modified SBA-15 in the presence of water vapor, Chem. Lett. 33 (2004) 510–511.

[19]   J. Duan, M. Higuchi, R. Krishna, T. Kiyonaga, Y. Tsutsumi, Y. Sato, et al., High $CO_2/N_2/O_2/CO$ separation in a chemically robust porous coordination polymer with low binding energy, Chem. Sci. 5 (2014) 660–666.

[20]   T. Ben, C. Pei, D. Zhang, J. Xu, F. Deng, X. Jing, et al., Gas storage in porous aromatic frameworks (PAFs), Energy Environ. Sci. 4 (2011) 3991–3999.

[21]   C.F. Martín, E. Stöckel, R. Clowes, D.J. Adams, A.I. Cooper, J.J. Pis, et al., Hypercrosslinked organic polymer networks as potential adsorbents for pre-combustion CO_2 capture, J. Mater. Chem. 21 (2011) 5475–5483.

[22]   Z. Xiang, X. Zhou, C. Zhou, S. Zhong, X. He, C. Qin, et al., Covalent-organic polymers for carbon dioxide capture, J. Mater. Chem. 22 (2012) 22663–22669.

[23]   Y. Zhao, Y. Shen, L. Bai, R. Hao, L. Dong, Synthesis and CO_2 adsorption properties of molecularly imprinted adsorbents, Environ. Sci. Technol. 46 (2012) 1789–1795.

[24]   V. Zelenák, M. Badaničová, D. Halamová, J. Čejka, A. Zukal, N. Murafa, et al., Amine-modified ordered mesoporous silica: Effect of pore size on carbon dioxide capture, Chem. Eng. J. 144 (2008) 336–342.

[25]   L. Chen, S. Xu, J. Li, Recent advances in molecular imprinting technology: current status, challenges and highlighted applications, Chem. Soc. Rev. 40 (2011) 2922–2942.

[26]   E.G. Derouane, Catalysts for Fine Chemical Synthesis: Microporous and Mesoporous Solid Catalysts, 1st ed., John Wiley & Sons, Ltd, West Sussex, UK, 2006.

[27]   R.G. Holdich, Fundamentals of particle technology, 1st ed., Midland Information Technology and Publishing, Loughborough, UK, 2002.

[28]   B. Brooks, Suspension polymerization processes, Chem. Eng. Technol. 33 (2010) 1737–1744.

[29]   R.G. Holdich, M.M. Dragosavac, G.T. Vladisavljević, E. Piacentini, Continuous membrane emulsification with pulsed (oscillatory) flow, Ind. Eng. Chem. Res. 52 (2012) 507–515.

[30]   E. Piacentini, E. Drioli, L. Giorno, Pulsed back-and-forward cross-flow batch membrane emulsification with high productivity to obtain highly uniform and concentrate emulsions, J. Membr. Sci. 453 (2014) 119–125.

[31]   G.T. Vladisavljević, R.A. Williams, Manufacture of large uniform droplets using

rotating membrane emulsfication, J. Colloid Interface Sci. 299 (2006) 396–402.

[32]   P.S. Silva, M.M. Dragosavac, G.T. Vladisavljević, H.C.H. Bandulasena, R.G. Holdich, M. Stillwell, et al., Azimuthally oscillating membrane emulsfication for controlled droplet production, AIChE J. 61 (2015) 3607–3615.

[33]   R.G. Holdich, M.M. Dragosavac, G.T. Vladisavljević, S.R. Kosvintsev, Membrane emulsification with oscillating and stationary membranes, Ind. Eng. Chem. Res. 49 (2010) 3810–3817.

[34]   G.H. Ma, C.J. An, H. Yuyama, Z.G. Su, S. Omi, Synthesis and characterization of polyurethaneurea–vinyl polymer (PUU–VP) uniform hybrid microspheres by SPG emulsification technique and subsequent suspension polymerization, J. Appl. Polymer Sci. 89 (2003) 163–178.

[35]   G.T. Vladisavljević, Structured microparticles with tailored properties produced by membrane emulsification, Adv. Colloid Interface Sci. 225 (2015) 53–87.

[36]   M.M. Dragosavac, M.N. Sovilj, S.R. Kosvintsev, R.G. Holdich, G.T. Vladisavljević, Controlled production of oil-in-water emulsions containing unrefined pumpkin seed oil using stirred cell membrane emulsification, J. Membr. Sci. 322 (2008) 178–188.

[37]   E. Egidi, G. Gasparini, R.G. Holdich, G.T. Vladisavljević, S.R. Kosvintsev, Membrane emulsification using membranes of regular pore spacing: Droplet size and uniformity in the presence of surface shear, J. Membr. Sci. 323 (2008) 414–420.

[38]   K.S.W. Sing, D.H. Everett, R.A.W. Haul, L. Moscou, R.A. Pierotti, J. Rouquérol, et al., REPORTING PHYSISORPTION DATA FOR GAS/SOLID SYSTEMS with special reference to the determination of surface area and porosity, Pure Appl. Chem.

57 (1985) 603–619.

[39]   D. Geldart, Types of gas fluidization, Powder Technol. 7 (1973) 285–292.

[40]   Z. Wang, M. Kwauk, H. Li, Fluidization of fine particles, Chem. Eng. Sci. 53 (1998) 377–395.

[41]   B. Sreenivasulu, I. Sreedhar, P. Suresh, K.V. Raghavan, Development trends in porous adsorbents for carbon capture, Environ. Sci. Technol. 49 (2015) 12641–12661.

[42]   H. A. Patel, S.H. Je, J. Park, D.P. Chen, Y. Jung, C.T. Yavuz, et al., Unprecedented high-temperature CO_2 selectivity in N_2-phobic nanoporous covalent organic polymers, Nat. Commun. 4 (2013) 1357–1364.

[43]   L. Wang, M. Yao, X. Hu, G. Hu, J. Lu, M. Luo, et al., Amine-modified ordered mesoporous silica: The effect of pore size on CO_2 capture performance, Appl. Surf. Sci. 324 (2015) 286–292.